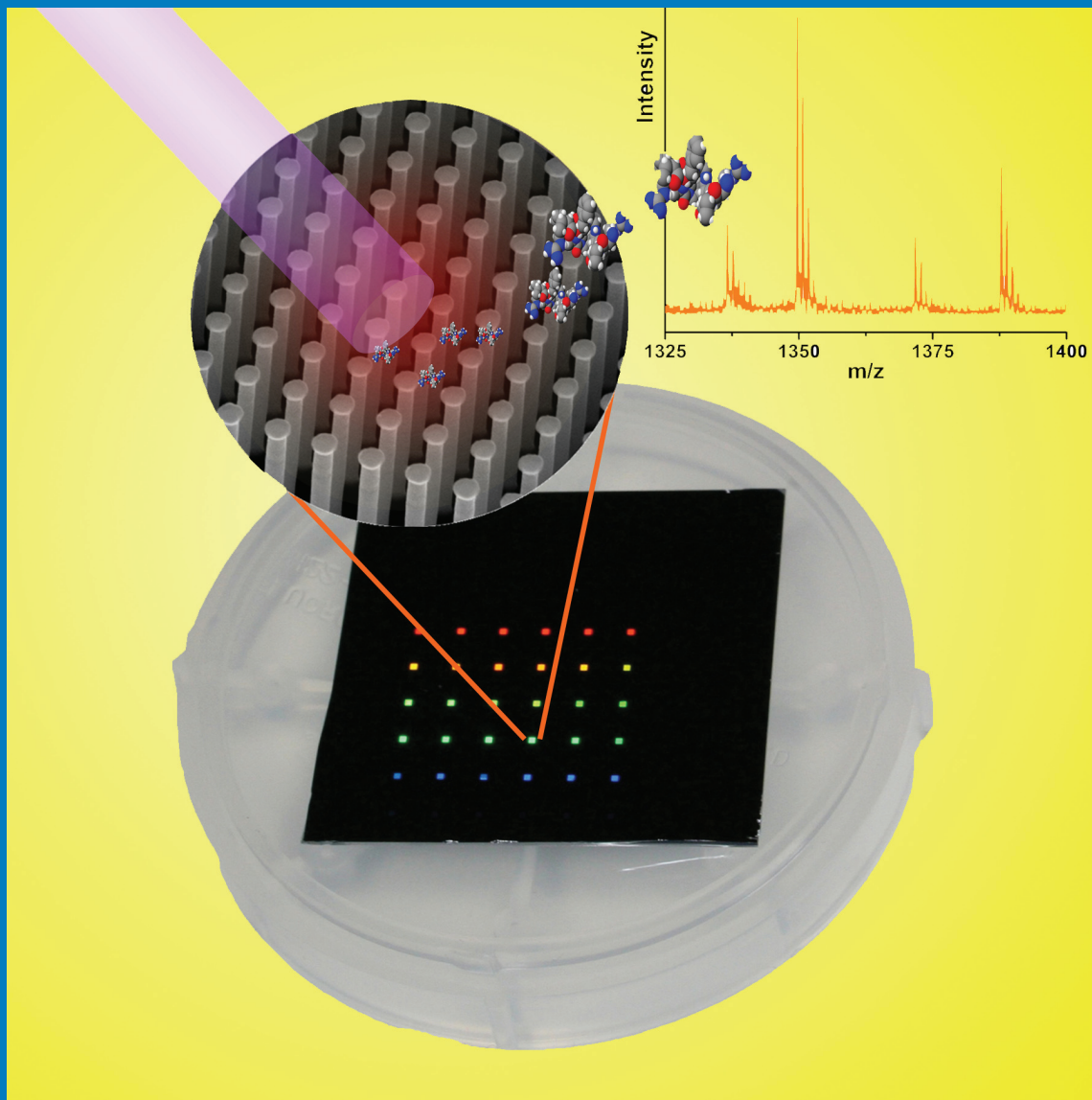


MARCH 25, 2010
VOLUME 114
NUMBER 11
pubs.acs.org/JPCC

THE JOURNAL OF PHYSICAL CHEMISTRY

C



Nanopost Arrays
Work as Nanophotonic
Ion Sources for the
Mass Spectrometry
of Biomolecules
(see page XA)

NANOMATERIALS, INTERFACES, HARD MATTER



ACS Publications
High quality. High impact.

www.acs.org

Tailored Silicon Nanopost Arrays for Resonant Nanophotonic Ion Production

Bennett N. Walker,^{†,§} Jessica A. Stolee,^{†,§} Deanna L. Pickel,[‡] Scott T. Retterer,[‡] and Akos Vertes^{*,†}

Department of Chemistry, George Washington University, Washington, D.C. 20052, Center for Nanophase Materials Sciences and Biosciences Division, Oak Ridge National Laboratory, Oak Ridge, Tennessee 37831

Received: November 19, 2009; Revised Manuscript Received: January 28, 2010

Nanostructures that have dimensions commensurate with the wavelength of the electromagnetic radiation exhibit near-field effects and, as optical antennas, can couple laser radiation to the local environment. Laser-induced silicon microcolumn arrays behave as nanophotonic ion sources that can be modulated by rotating the plane of light polarization. However, the limited range of surface morphologies available for these substrates makes it difficult to study the underlying mechanism that governs ion production. Here we demonstrate that nanopost arrays (NAPAs) can be tailored to exhibit resonant ion production. Ion yields from posts with subwavelength diameter show sharp resonances at high aspect ratios. The resonant enhancement in ion intensities can be modulated by adjusting the periodicity. In addition to strong molecular ion formation, the presence of high-energy fragmentation channels is observed. Ion yields from NAPAs exhibit dramatic differences for p- and s-polarized laser beams, indicating that energy coupling is similar to antenna arrays. These nanophotonic ion sources can control the degree of ion fragmentation and could eventually be integrated with micromachined mass spectrometers and microfluidic devices.

Introduction

Quasiperiodic columnar silicon nanostructures offer low reflectivity in a wavelength range spanning from 200 nm through the mid-IR¹ to the terahertz region.² Examples include laser-induced silicon microcolumn arrays (LISMAs)³ produced by ultrafast laser surface structuring⁴ and silicon nanotip (SiNT) arrays fabricated by plasma etching.² These high aspect ratio structures offer sub-band gap light absorption with a corresponding photocurrent, broadband antireflection properties, efficient electron emission⁵ and superhydrophobic behavior.⁶

Nanoscale protrusions on silicon surfaces are known to result in the local enhancement of electromagnetic radiation that, for a 10:1 aspect ratio column, can reach an intensity gain close to 200 in the near field.⁷ Metal nanostructures can exhibit additional enhancements through surface plasmon resonances and operate as optical antennas.^{8–10} These structures demonstrate resonant energy absorption¹¹ that is sensitive to polarization¹² and antenna length,⁹ and their near-field response can be tuned through altering their geometry.¹³ Near-field radiation induced fluorescence has been demonstrated in biological membranes¹⁴ and single molecules¹⁵ opening the way for the microscopy and spectroscopy of subwavelength domains. At higher laser fluences materials brought to the proximity of these enhanced fields can undergo ablation^{16,17} that can include the nanoscopic structure producing the enhancement itself.¹⁸ In particular, gold nanoparticle ablation induced by the near field sets in between 9 and 12 mJ/cm², whereas melting only commences at 15 mJ/cm².¹⁸

Nanostructures that have dimensions commensurate with the wavelength of the electromagnetic radiation exhibit near-field

effects^{19,20} and, as optical antennas, can couple laser radiation to the local environment.²¹ We have recently discovered that increasing the laser intensity on LISMA structures covered with biomolecules results in adsorbate ion production,³ and this process exhibits nanophotonic behavior.²² Features of ion production from LISMAs include polarization and incidence-angle-dependent ion yields and the ability to adjust the degree of ion fragmentation through the laser fluence.^{3,22} As the laser intensity is increased, structure specific fragment ions resulting from both low energy and high-energy processes are observed.²³ These results indicate that surface collisions, in-plume reactions, and the enhancement of the electromagnetic field near the microcolumns may all play a role in ion production from these sources. Because of the narrow range of array geometries accessible through laser surface structuring,²⁴ there are limited possibilities for tuning the interaction between the LISMA structure and the laser radiation.

Silicon nanopost arrays (NAPAs) are similar to LISMAs in their chemical composition and overall morphology. Because of the nanofabrication used in their production, however, we have a greater control over the relevant dimensions. The schematic of a NAPA, along with the relevant dimensions and the electric field of the incident laser beam is shown in Figure 1A.

In this work, we explore laser desorption ionization from tailored NAPAs produced by nanofabrication in a wide range of post diameters, heights, and periodicities. Ion production from NAPA structures upon exposure to laser radiation was explored for a range of dimensions and laser fluences. Our results show that selecting certain post aspect ratios give rise to a resonance in ion production.

Experimental Section

NAPA Fabrication. Low resistivity (0.001–0.005 $\Omega \cdot \text{cm}$) p-type silicon wafers were spin-coated by ZEP520A resist at 6000 rpm for 45 s and baked at 180 °C for 2 min. A variety of

* Corresponding author. Address: 725 21st Street, N.W., Washington, D.C. 20052. Phone: (202) 994-2717. Fax: (202) 994-5873. E-mail: vertes@gwu.edu.

[†] George Washington University.

[‡] Oak Ridge National Laboratory.

[§] These authors contributed equally to this work.

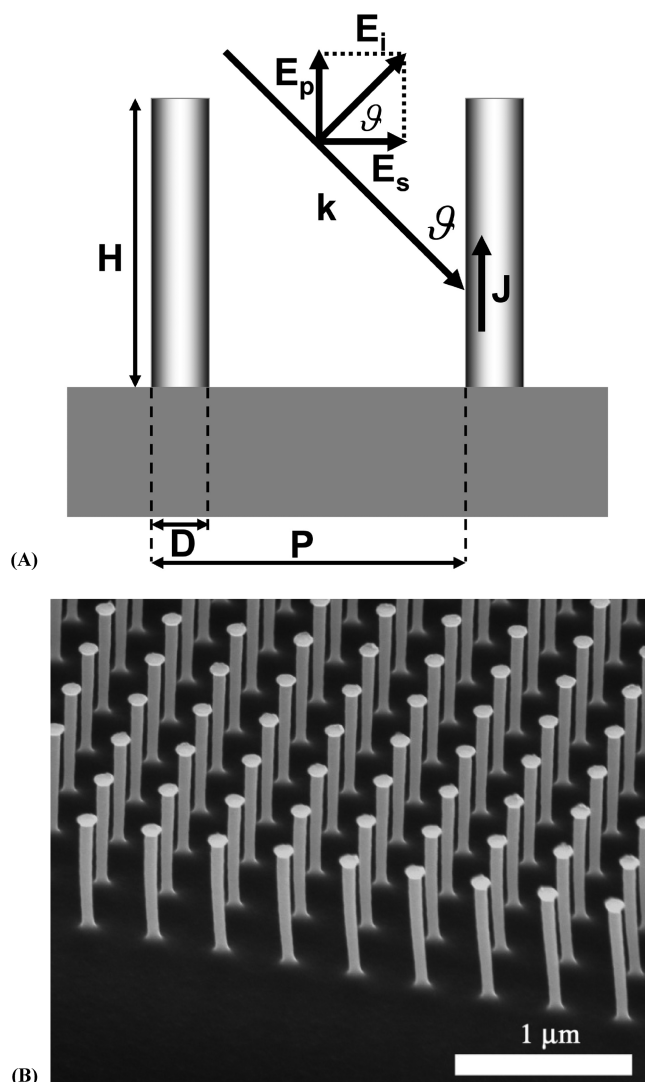


Figure 1. (A) Schematic of NAPA with post height, H , diameter, D , and periodicity, P , indicates the relationship between the electric field vector of the incident laser beam propagating in \mathbf{k} direction, E_i , its orthogonal projections, and the current, \mathbf{J} , induced in the post. (B) SEM image of a NAPA segment with $D = 100$ nm, $H = 1,000$ nm, and $P = 350$ nm shows uniform periodicity and height. The posts have vertical walls with minimum tapering.

rectangular packed patterns for cylindrical NAPA were produced by e-beam lithography (JEOL JBX-9300). Nanopost diameters and periodicities were systematically varied from 50 to 600 nm, and from 200 to 1200 nm, respectively. To remove the exposed resist, wafers were soaked in xylenes for 30 s, rinsed with isopropanol, and blow dried with nitrogen gas. The wafer was descummed in oxygen plasma at 100 W for 6 s using a Technics reactive ion etching (RIE) system. A 10-nm chromium layer was deposited onto the wafer at a rate of 0.1 nm/s using an electron beam evaporator. Sonication of the wafer in an acetone bath for 2.5 min dissolved the unexposed resist and removed the chromium layer from those areas. Various nanopost heights (~ 200 nm to ~ 1500 nm) were produced at a rate of ~ 100 nm/min by an Oxford PlasmaLab100 RIE system using a combination of C_4F_8 and SF_6 gases. The integrity and the dimensions of the resulting NAPA were inspected using a scanning electron microscope (SEM; FEI Nova Nanolab 600 DualBeam) system (see Figure 1B).

Mass Spectrometry. Following the nanofabrication process, the laser desorption ionization properties of the NAPA were

confirmed using a Bruker Daltonics Autoflex II reflectron time-of-flight mass spectrometer (TOF-MS). Adsorbate solutions of substance P, bradykinin, leucine enkephalin, angiotensin I, GFL, and verapamil were prepared at a concentration of ~ 1 mg/mL in 50% methanol. A $0.5 \mu\text{L}$ aliquot of a solution was deposited onto the NAPA surface and air-dried. Averaged mass spectra were acquired from 100 laser shots in reflectron mode. More detailed experiments, aimed at the fluence dependence of the ion yield and the fragmentation behavior, were conducted on a Kratos Axima III TOF-MS with a curved field reflectron. The Kratos instrument used a nitrogen laser focused to $\sim 100 \mu\text{m}$ diameter spot with adjustable laser fluence on the NAPA target. Averaged spectra were acquired from 200 laser shots in reflectron mode using a 2.5 kV extraction voltage with a 100 ns delay and a 20 kV accelerating voltage.

Polarized Laser Desorption Ionization. Radiation from an LSI nitrogen laser (VSL-337ND) was polarized using an uncoated Glan-Taylor calcite polarizer in a rotation mount. The 4 ns laser pulses were attenuated with a continuously variable neutral density filter to maintain a pulse energy of $\sim 10 \mu\text{J}$, while the plane of polarization was rotated between s- and p-polarized. The polarized beam was focused with a fused silica lens to a $\sim 200 \mu\text{m}$ spot on the NAPA structures in the source region of a home-built TOF-MS.

Energy Deposition Modeling. To model the energy deposition and redistribution in the nanoposts, a three-dimensional finite difference scheme was implemented with an adaptive mesh. With the help of the FlexPDE 6.06 (PDE Solutions, Inc.) package, eq 2 was solved for a single post with insulating boundary conditions, except for the base of the post, where heat conduction to the silicon wafer was allowed. The laser pulse was represented by a uniform intensity distribution of 6×10^6 W/cm² along the post. The thermal conductivity and specific heat of silicon were treated as temperature-dependent parameters.

Results and Discussion

NAPA Production. The cylindrical post diameters, D , heights, H , and periods, P , are varied in the $D = 50$ –600 nm, $H = 200$ –1500 nm, and $P = 200$ –1200 nm ranges, respectively. The arrays are established on a rectangular grid of $500 \mu\text{m}$ on each side. Thus the array sizes are $2500 \times 2500 = 6\,250\,000$ posts for $P = 200$ nm, and $416 \times 416 = 173\,056$ posts for $P = 1200$ nm. Figure 1B shows the SEM image of a segment of the NAPA produced by anisotropic RIE which achieves uniform post heights with vertical walls and minimum tapering. The 10 nm thick chromium top on the posts is necessary for the RIE process that produces posts with aspect ratios up to $H/D = 15$. To rule out the possible effect of these chromium caps on the nanophotonic behavior, we refer to similar findings in the case of LISMA structures. Those systems do not have chromium caps, yet they exhibit many similar nanophotonic properties, such as the polarization-dependent ion yields discussed below.

Laser Desorption Ionization Mass Spectra from NAPA. Small organics and biomolecules, deposited on the NAPA structures, are efficiently desorbed and ionized by 337 nm nitrogen laser radiation of ~ 20 mJ/cm² and above. Figure 2A depicts the high mass region of the low fluence mass spectrum of the neuropeptide substance P (RPKPQQFFGLM). The peptide sequences are described by one-letter code, and the fragmentation nomenclature follows the conventions introduced by Biemann.²⁵ Protonated molecules are produced with high abundance accompanied by low amounts of alkalinated products and a fragment corresponding to m/z 14 loss. In the low mass

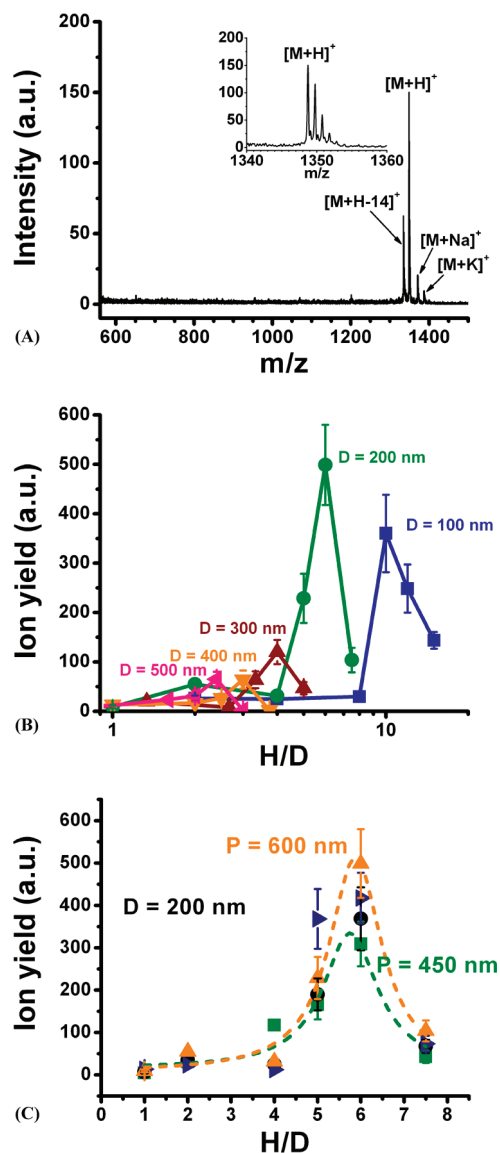


Figure 2. (A) Molecular ions in the mass spectrum of substance P produced on NAPAs at low laser fluences. The inset shows the $[M+H]^+$ isotope distribution that corresponds to the calculated pattern. (B) Substance P ion yields as a function of post aspect ratios show strong maxima for slender posts. (C) For a given diameter ($D = 200$ nm), at the optimum aspect ratio, $H/D = 6$, increasing periodicity, $P = 450$ nm (■), 500 nm (●), 550 nm (▲), and 600 nm (▲), results in higher ion yields. Lorentzian fits for $P = 450$ and 600 nm represent the data with $R^2 = 0.94$ and 0.98 regression coefficients, respectively.

region ($m/z < 560$), backbone cleavage (a_2 , b_2), internal fragments (PK-28/KP-28, QF, KPQ-28), and immonium ions (R-87 or P-17, K/Q, K/Q-28, M-28, R-45, F-28, K/Q-45) are prevalent. Other small peptides (bradykinin [RPPGFSPFR], leucine enkephalin [YGGFL], angiotensin I [DRVYIHPFHL], GFL, etc.) give similar results.

Small organics composed of preformed ions (organic salts), such as verapamil hydrochloride, produce very clean spectra (not shown) dominated by the protonated molecule, with negligible fragmentation corresponding to the loss of the 3,4-dimethoxyphenylmethyl moiety. Preformed ions exist as charged entities already in the solid phase or as an adsorbate. Thus they do not require an ionization step and can be used to probe the desorption process separately. The desorption of verapamil from the NAPA structure is found to be very efficient resulting in an ultralow detection limit of 6 amol.

The reusability of NAPAs was investigated by taking mass spectra of various peptides repeatedly from the same substrate and sonicating it in methanol and water baths between the experiments. Our results showed minimal cross contamination between runs, and no nanopost damage was observed after sonication. The minor cross contamination is likely due to the ultra low limit of detection, pointing to the importance of thorough cleaning between experiments. Furthermore, storage of the NAPA structures for over 1.5 years did not impact the performance of these structures. These results indicate the potential for reusability for these structures and stability in the ambient environment.

Resonant Ion Production and Fragmentation. To explore the impact of NAPA geometries on peptide ion production, the yields of quasimolecular ions are followed for a variety of nanofabricated structures. Of the three main parameters, D , H , and P , the post heights have the strongest influence on the ion yields. Figure 2B shows the yields of substance P ions as a function of the post aspect ratio, H/D , for different post diameters. Compared to the $H/D = 1$ case, the large diameter posts, $D = 500$ and 400 nm, have modest ion yield maxima at the low aspect ratios of 2.4 and 3, respectively, that show a factor of 7 increase. As the posts become thinner, $D = 300$, 200 , and 100 nm, the maxima shift to higher aspect ratios, $H/D = 4$, 6 , and 10 , respectively, and the ion yields show more dramatic gains. The largest gain, a factor of 55 compared to the $H/D = 1$ case, is observed for $D = 200$ nm at an aspect ratio of 6. In terms of post height, the $D = 500$, 400 , 300 , and 200 posts show maximum ion yields at $H = 1200$ nm, and the $D = 100$ nm post is most efficient at $H = 1000$ nm. This corresponds to $H/\lambda \approx 3.0$ to 3.6 and an optimum gain of 55.

This resonance-like behavior is analogous to the aspect-ratio-dependent gains in the near-field intensity observed for spheroidal silicon protrusions through fluorescence.^{7,26} Studying the effect of probe length on field enhancement around an apertureless near-field probe, Bohn and co-workers found that for a tip radius of curvature $R_c = 10$ nm, the intensity enhancement of $\kappa^2 \approx 225$ is the highest at $a/R_c \approx 12$, where a is the semimajor axis length of the spheroid. They attributed the drop-off of the enhancement at higher aspect ratios to the emergence of internal resonances in the probe. For the protrusion with $R_c = 5$ nm, the enhancement factor continues to grow up to $\kappa^2 \approx 250$ at $a/R_c \approx 20$, the highest studied aspect ratio. The general trend in this data is similar to our ion yield observations. Slender posts in both cases produce strong enhancement in the signal at aspect ratios that shift to higher values for smaller diameters. Despite the similarities, the interactions of the posts with the laser radiation are significantly different in the two studies. This is directly manifested in the corresponding skin depth, δ , values. While the silicon in the fluorescence study has a skin depth of ~ 1100 nm, i.e., their near-field probe is practically transparent, in our work, $\delta \approx 84$ nm resulting in strong absorption of the incident light in the posts. Further differences arise from the interactions between the posts in our large arrays.

To uncover the effect of periodicity on the ion yields, arrays of $D = 200$ nm posts and different periods, $P = 450$, 500 , 550 , and 600 nm, are compared as a function of the aspect ratio. The results for substance P are summarized in Figure 2C. All four arrays produce maximum ion yields at $H/D \approx 6$, but the amplitudes of the gains, 18 and 30 for $P = 450$ and 600 nm, respectively, are somewhat different. This modest dependence on the period indicates that most of the

TABLE 1: Fragmentation of Small Peptides in Laser Desorption Ionization from NAPA Substrates^a

Peptides	fragment ions ^b								
	quasi-molecular ions	14 loss	a ions	b ions	c ions	y ions	Y ions	internal fragments	immonium ions ^c
GFL	M+H, M+Na, M+K	M+H-14	a ₂	b ₂	c ₂	y ₁ , y ₂	Y1		F-28
substance P	M+H, M+Na, M+K	M+H-14	a ₂ , a ₂ -NH ₃	b ₂	c ₂			PKPQQ-28, PQQ, KPQ-28	R-87 or P-17, K/Q, K/Q-28, M-28, R-45, F-28, K/Q-45

^a $D = 200$ nm, $H = 1000$ nm, and $P = 500$ nm for substance P, and $D = 200$ nm, $H = 800$ nm, and $P = 500$ nm for GFL. ^b The peptide fragmentation nomenclature follows the conventions introduced by Biemann.²⁵ ^c Immonium ions undergo consecutive losses of 17, 12, 29, etc. This notation starts from the intact immonium ion of a residue and marks the losses in nominal mass units.

enhancement is caused by near-field effects around a post that are only weakly influenced by the presence of other posts in the array.

The two most significant factors that influence the desorption and ionization of adsorbates are the near-field enhancement of the laser intensity and the heating of the posts by the radiation. The electric field, \mathbf{E} , at a distance r from the surface of the post can be approximated as⁷ $\mathbf{E} = -\kappa|\mathbf{E}_p|(D/(D+2r))^3\mathbf{r}$ and $\mathbf{E}_p = \mathbf{E}_i \sin \theta \cos \phi$, where \mathbf{E}_p is the component of the laser electric field vector that is parallel with the posts, θ is the angle of incidence, ϕ is the polarization angle, and \mathbf{r} is a unit vector pointing away from the post. Thus, the enhanced laser intensity at the top of the post decays as $I(r)$:

$$I(r) = -\kappa^2 I_i \sin^2 \theta \cos^2 \phi \left(\frac{D}{D+2r} \right)^6 \quad (1)$$

where I_i is the incident laser intensity. Therefore, the enhanced intensity depends on the angle of incidence and the polarization angle, and decays rapidly with the distance from the surface.

Adsorbates close to the surface experience strong electric fields and radiation intensities that, depending on the aspect ratio of the posts, can be up to 200 times higher than the incident laser intensity. These conditions can promote ionization and induce fragmentation through a yet unknown mechanism. Table 1 summarizes the fragment ions produced by a nitrogen laser pulse on a typical NAPA from model peptides GFL and substance P. In addition to some of the **a**, **b**, and **y**-series ions commonly observed in high energy collision-activated dissociation (CAD)²⁷ and in surface-induced dissociation (SID),²⁸ the decomposition products observed from NAPA include internal fragments and immonium ions. In place of the commonly observed ammonia loss from the protonated molecule at low energies, a loss of 14 Da is detected. On the basis of the size distribution and the nature of the fragments, it seems that low-energy and high-energy decomposition channels are operational simultaneously. Currently only nanophotonic ionization techniques, LISMA and NAPA, produce peptide molecular ions and their structure specific fragments without additional ion activation.

Polarization-Dependent Ion Yields. It has been shown that polarization and incidence-angle-dependent strong optical fields can be generated between a sharp metal tip and a surface.²⁹ Even without plasmon resonance, strong field enhancement is observed for p-polarized light, whereas s-polarized beams produce no enhancement. Polarization dependent ion production has also been demonstrated for LISMA substrates.²² Here we show that laser desorption ionization from the NAPA structures at constant fluence exhibits strong polarization angle dependence. Figure 3 summarizes the results for the ion yields of

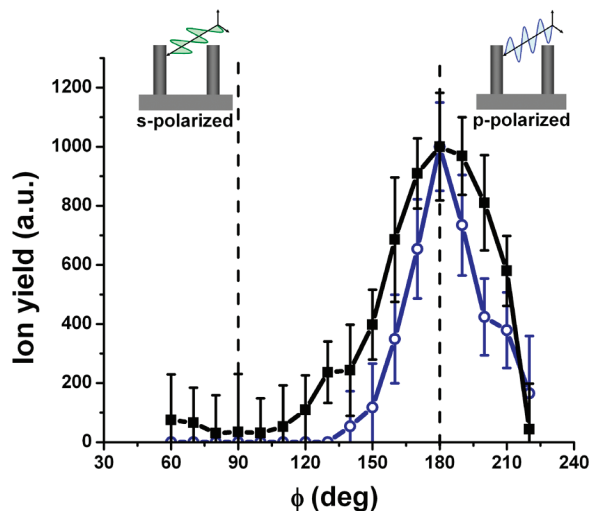


Figure 3. Normalized ion yields of verapamil (■) and bradykinin (○) as a function of polarization angle, ϕ , at a constant fluence (24 mJ/cm²). Ion production seems to be a threshold process.

verapamil and bradykinin as a function of ϕ between 60° and 220°. Verapamil follows a close to $\cos^2 \phi$ behavior, with strong ion production for p-polarized light and close to zero ion yields for s-polarized radiation. Although the general trend is similar, bradykinin and angiotensin I (not shown) ion yields approximate a cusp in the p-polarized region and drop to zero in a wide range (from 60° to 130°) around the s-polarized orientation. Since verapamil exists in ionic form already as an adsorbate, ion production only requires a desorption step, whereas, for the peptides, an ionization step, e.g., proton transfer, is also required. This additional ionization step needed for peptides might be responsible for the differences in the shapes of the ion yield curves in Figure 3.

Modeling of Energy Deposition. Ion production from adsorbates on NAPAs can be rationalized by the onset of several processes: energy concentration and deposition induced by the interaction of the laser radiation with the NAPA, energy redistribution in the quasi one-dimensional posts, and the desorption, ionization, and activation of the adsorbed species. Energy deposition into the nanoposts is governed by the power dissipation in their volume, $dP/dV = \mathbf{J} \cdot \mathbf{E}_i$, where $\mathbf{J} = \sigma \cdot \mathbf{E}_p$ is the current induced by the electric field in the posts, and σ is their conductivity. The penetration of the electric field into the posts, and therefore the region with significant current and dissipation, is determined by the skin depth, which for our low resistivity silicon at 337 nm wavelength is 84 nm. The surface current, \mathbf{J}_s , decays with the distance, d , from the surface as $\mathbf{J} = \mathbf{J}_s \exp(-d/\delta)$. Thus, to follow the energy redistribution, the heat conduction equation has to be solved for a penetrating volume source. For posts thinner than the phonon mean free path, which for silicon nanoposts at 300 K is ~ 800 nm,³⁰ the Fourier heat conduction equation is replaced by the ballistic-diffusive heat transport equation. The difference between the two approaches

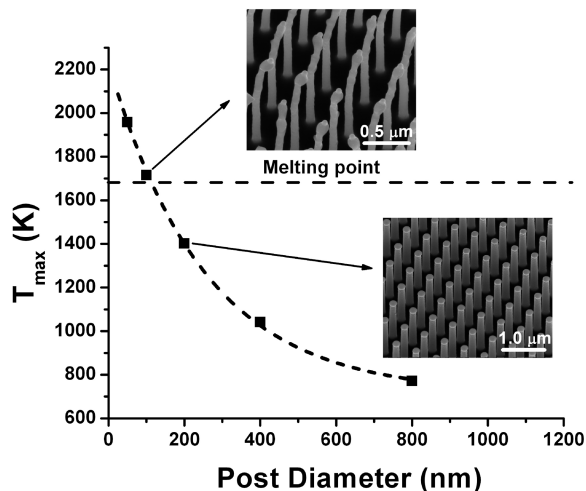


Figure 4. After irradiation by a $\tau = 5$ ns laser pulse of 6×10^6 W/cm² power density, calculated silicon nanopost surface temperatures show a strong dependence on the post diameter in the submicrometer range. The SEM images in the insets indicate that posts with ~ 100 nm diameter exhibit signs of transient melting.

is most pronounced at short time scales,^{31,32} so for the calculation of the post surface temperatures at the end of the laser pulse we use the former.

$$\frac{\partial T}{\partial t} = \nabla \cdot \left(\frac{K(T)V}{C_p} \nabla T \right) + (1 - R) \frac{V}{\delta C_p} I_i \sin^2 \theta \cos^2 \varphi \exp(-d/l\delta) \quad (2)$$

where $K(T)$, C_p , R , and V are the temperature-dependent thermal conductivity, heat capacity, reflectance, and molar volume, respectively. The FlexPDE finite element package is used with an adaptive mesh to solve eq 2 for the nanopost geometry. Surface temperatures, T_{surf} , are calculated on the irradiated side of the nanopost at the end of the laser pulse. For $D = 300$ nm posts, the results indicate that the surface temperature is a strong function of the polarization angle. At 24 mJ/cm², temperatures for p-polarized light reach 1228 K, whereas no heating is predicted for s-polarized radiation. Figure 3 indicates that the ion production is a threshold process, with an earlier onset for verapamil that requires only a desorption step compared to bradykinin that relies on an additional ionization step for ion production. Compared to verapamil, the relative ion yield values at the maximum are $1.4 \times$ lower for bradykinin and $1.6 \times$ lower for angiotensin I.

Modeling based on eq 2 also demonstrates that NAPA with thinner posts reach increasingly higher surface temperatures. This effect sets in as the post diameters become smaller than the heat diffusion length, l , in silicon. Due to the temperature dependence of K and C_p , for a $\tau = 5$ ns laser pulse $l = (\bar{K}(T)V\tau/C_p)^{1/2}$ drops from 730 nm at 300 K to 230 nm at 1600 K. Figure 4 demonstrates that, based on eq 2, indeed, at a laser fluence of 30 mJ/cm², the surface temperature of 100-nm diameter posts temporarily exceeds the melting point. SEM images of NAPAs, after exposure to laser radiation, confirm this prediction (see insets in Figure 4).

Conclusions

Nanophotonic ion production was first demonstrated on LISMA substrates.²² Strong field enhancements near the nano-

posts are thought to contribute to ion formation. Because of the limitations of the laser surface processing involved in their production, those structures are restricted to diameters of 300 nm and above and maximum aspect ratios of 2. Nanofabrication of NAPAs can produce structures with 3 times smaller diameters and with aspect ratios up to $H/D = 15$. These higher aspect ratio structures have significantly increased local fields that can promote ionization. Laser desorption ionization experiments show resonant ion production from these slender posts with a 55-fold enhancement.

In addition, a dramatic increase of the ion yield is observed as the angle of polarization transitions from the s- to p-polarized, indicating a similarity to antenna arrays. The strong polarization dependence of the ion yields from NAPA enables the rapid modulation and switching of ion production.

The diameter of slender posts is close to the heat diffusion length. Therefore, these posts reach higher surface temperatures and can more efficiently transfer energy to the adsorbate. As a result, NAPA-based ion sources offer adjustable fragmentation not available for ion sources currently used in the structure elucidation of peptides and proteins. The traditional techniques rely on CAD or other ion activation techniques to produce structure specific fragments.

Further development and understanding of these nanophotonic ion sources can lead to a highly efficient ion source capable of controlling the degree of fragmentation for various biomolecules. The size, material and fabrication of NAPA structures make them amenable to eventual integration with microfluidic devices and micromachined mass spectrometers.

Acknowledgment. Financial support by the Chemical Sciences, Geosciences and Biosciences Division within the Office of Basic Energy Sciences of the U.S. Department of Energy (DE-FG02-01ER15129) and from Protea Biosciences, Inc. is acknowledged. B.N.W. and J.A.S. are grateful for the scholarship award from the Achievement Rewards for College Scientists Foundation, Inc. (ARCS). The NAPA structures were nanofabricated, and a portion of the mass spectrometry data was obtained in the framework of a User Agreement (CNMS2008-249) at Oak Ridge National Laboratory's Center for Nanophase Materials Sciences, sponsored by the Scientific User Facilities Division, Office of Basic Energy Sciences, U.S. Department of Energy.

References and Notes

- (1) Crouch, C. H.; Carey, J. E.; Warrender, J. M.; Aziz, M. J.; Mazur, E.; Genin, F. Y. *Appl. Phys. Lett.* **2004**, *84*, 1850.
- (2) Huang, Y. F.; Chattopadhyay, S.; Jen, Y. J.; Peng, C. Y.; Liu, T. A.; Hsu, Y. K.; Pan, C. L.; Lo, H. C.; Hsu, C. H.; Chang, Y. H.; Lee, C. S.; Chen, K. H.; Chen, L. C. *Nat. Nanotechnol.* **2007**, *2*, 770.
- (3) Chen, Y.; Vertes, A. *Anal. Chem.* **2006**, *78*, 5835.
- (4) Her, T. H.; Finlay, R. J.; Wu, C.; Deliwala, S.; Mazur, E. *Appl. Phys. Lett.* **1998**, *73*, 1673.
- (5) Zorba, V.; Tzanetakakis, P.; Fotakis, C.; Spanakis, E.; Stratakis, E.; Papazoglou, D. G.; Zergioti, I. *Appl. Phys. Lett.* **2006**, *88*, 081103.
- (6) Zorba, V.; Persano, L.; Pisignano, D.; Athanassiou, A.; Stratakis, E.; Cingolani, R.; Tzanetakakis, P.; Fotakis, C. *Nanotechnology* **2006**, *17*, 3234.
- (7) Hamann, H. F.; Gallagher, A.; Nesbitt, D. J. *Appl. Phys. Lett.* **2000**, *76*, 1953.
- (8) Farahani, J. N.; Pohl, D. W.; Eisler, H. J.; Hecht, B. *Phys. Rev. Lett.* **2005**, *95*, 017402.
- (9) Muhlschlegel, P.; Eisler, H. J.; Martin, O. J. F.; Hecht, B.; Pohl, D. W. *Science* **2005**, *308*, 1607.
- (10) Cubukcu, E.; Kort, E. A.; Crozier, K. B.; Capasso, F. *Appl. Phys. Lett.* **2006**, *89*, 3.
- (11) Crozier, K. B.; Sundaramurthy, A.; Kino, G. S.; Quate, C. F. *J. Appl. Phys.* **2003**, *94*, 4632.
- (12) Fischer, H.; Martin, O. J. F. *J. Eur. Opt. Soc., Rapid Publ.* **2008**, *3*, 08018.

- (13) Merlein, J.; Kahl, M.; Zuschlag, A.; Sell, A.; Halm, A.; Boneberg, J.; Leiderer, P.; Leitenstorfer, A.; Bratschitsch, R. *Nat. Photonics* **2008**, *2*, 230.
- (14) Sanchez, E. J.; Novotny, L.; Xie, X. S. *Phys. Rev. Lett.* **1999**, *82*, 4014.
- (15) Anger, P.; Bharadwaj, P.; Novotny, L. *Phys. Rev. Lett.* **2006**, *96*, 113002.
- (16) Stockle, R.; Setz, P.; Deckert, V.; Lippert, T.; Wokaun, A.; Zenobi, R. *Anal. Chem.* **2001**, *73*, 1399.
- (17) Hwang, D. J.; Chimmalgi, A.; Grigoropoulos, C. P. *J. Appl. Phys.* **2006**, *99*, 044905.
- (18) Plech, A.; Kotaidis, V.; Lorenc, M.; Boneberg, J. *Nat. Phys.* **2006**, *2*, 44.
- (19) Girard, C. *Rep. Prog. Phys.* **2005**, *68*, 1883.
- (20) Coyle, S.; Netti, M. C.; Baumberg, J. J.; Ghanem, M. A.; Birkin, P. R.; Bartlett, P. N.; Whittaker, D. M. *Phys. Rev. Lett.* **2001**, *87*, 176801.
- (21) Taminiou, T. H.; Stefani, F. D.; Segerink, F. B.; Van Hulst, N. F. *Nat. Photonics* **2008**, *2*, 234.
- (22) Walker, B. N.; Razunguzwa, T.; Powell, M.; Knochenmuss, R.; Vertes, A. *Angew. Chem., Int. Ed.* **2009**, *48*, 1669.
- (23) Stolee, J. A.; Chen, Y.; Vertes, A. *J. Phys. Chem. C* [Online early access]. DOI: 10.1021/jp906834z. Published online Oct 19, 2009.
- (24) Akhmanov, S. A.; Emelyanov, V. I.; Koroteyev, N. I.; Seminogov, V. N. *Usp. Fiz. Nauk* **1985**, *147*, 675.
- (25) Biemann, K. *Biomed. Environ. Mass Spectrom.* **1988**, *16*, 99.
- (26) Bohn, J. L.; Nesbitt, D. J.; Gallagher, A. *J. Opt. Soc. Am. A* **2001**, *18*, 2998.
- (27) Vachet, R. W.; Winders, A. D.; Glish, G. L. *Anal. Chem.* **1996**, *68*, 522.
- (28) Nair, H.; Somogyi, A.; Wysocki, V. H. *J. Mass Spectrom.* **1996**, *31*, 1141.
- (29) Martin, O. J. F.; Girard, C. *Appl. Phys. Lett.* **1997**, *70*, 705.
- (30) Luo, G. H.; Chen, Y.; Daniels, H.; Dubrow, R.; Vertes, A. *J. Phys. Chem. B* **2006**, *110*, 13381.
- (31) Chen, G. *Phys. Rev. Lett.* **2001**, *86*, 2297.
- (32) Joshi, A. A.; Majumdar, A. *J. Appl. Phys.* **1993**, *74*, 31.

JP9110103